

Generalized receptor law governs phototaxis in the phytoplankton *Euglena gracilis*

Andrea Giometto^{a,b,1}, Florian Altermatt^{b,c}, Amos Maritan^d, Roman Stocker^e, and Andrea Rinaldo^{a,f,1}

^aLaboratory of Ecohydrology, School of Architecture, Civil and Environmental Engineering, École Polytechnique Fédérale de Lausanne, CH-1015 Lausanne, Switzerland; ^bDepartment of Aquatic Ecology, Eawag: Swiss Federal Institute of Aquatic Science and Technology, CH-8600 Dübendorf, Switzerland; ^cInstitute of Evolutionary Biology and Environmental Studies, University of Zurich, CH-8057 Zurich, Switzerland; ^dDipartimento di Fisica e Astronomia, Università di Padova, I-35131 Padua, Italy; ^eRalph M. Parsons Laboratory, Department of Civil and Environmental Engineering, Massachusetts Institute of Technology, Cambridge, MA 02139; and ^fDipartimento di Ingegneria Civile, Edile ed Ambientale, Università di Padova, I-35131 Padua, Italy

Edited by Edward F. DeLong, University of Hawaii, Manoa, Honolulu, HI, and approved April 15, 2015 (received for review December 1, 2014)

Phototaxis, the process through which motile organisms direct their swimming toward or away from light, is implicated in key ecological phenomena (including algal blooms and diel vertical migration) that shape the distribution, diversity, and productivity of phytoplankton and thus energy transfer to higher trophic levels in aquatic ecosystems. Phototaxis also finds important applications in biofuel reactors and microbiopropellers and is argued to serve as a benchmark for the study of biological invasions in heterogeneous environments owing to the ease of generating stochastic light fields. Despite its ecological and technological relevance, an experimentally tested, general theoretical model of phototaxis seems unavailable to date. Here, we present accurate measurements of the behavior of the alga *Euglena gracilis* when exposed to controlled light fields. Analysis of *E. gracilis*' phototactic accumulation dynamics over a broad range of light intensities proves that the classic Keller–Segel mathematical framework for taxis provides an accurate description of both positive and negative phototaxis only when phototactic sensitivity is modeled by a generalized “receptor law,” a specific nonlinear response function to light intensity that drives algae toward beneficial light conditions and away from harmful ones. The proposed phototactic model captures the temporal dynamics of both cells' accumulation toward light sources and their dispersion upon light cessation. The model could thus be of use in integrating models of vertical phytoplankton migrations in marine and freshwater ecosystems, and in the design of bioreactors.

phototactic potential | photoresponse | sensory system |
photoaccumulation | microbial motility

Microorganisms possess a variety of sensory systems to acquire information about their environment (1), including the availability of resources, the presence of predators, and the local light conditions (2). For any sensory system, the system's response function determines the organism's capability to process the available information and turn it into a behavioral response. Such a response function is shaped by the natural environment and its fluctuations (3–5) and affects the search strategy [be it mate search, food search, etc. (6, 7)] and the swimming behavior of microorganisms (8). Gradient sensing is particularly important in marine and freshwater ecosystems, where the distribution of resources is highly heterogeneous (9, 10) and the ability to move toward resource hot spots can provide a strong selective advantage to motile organisms over nonmotile ones (2, 5). Spatiotemporal patterns of light underwater contribute to the heterogeneity of the aquatic environment. Because light is a major carrier of energy and information in the water column (11), phototaxis is a widespread case of directed gradient-driven locomotion (12, 13), found in many species of phytoplankton and zooplankton. Phototaxis strongly affects the ecology of aquatic ecosystems, contributing to diel vertical migration of phytoplankton, one of the most dramatic migratory phenomena on Earth and the largest in terms of biomass (14). Diel vertical migration is crucial for the survival and proliferation of plankton (13, 15, 16), may affect the structuring of algal blooms (17), and allows plankton to escape from predation by filter-feeding

organisms. Because phytoplankton are responsible for one-half of the global photosynthetic activity (18, 19) and are the basis of marine and freshwater food webs (20), their behavior and productivity have strong implications for ocean biogeochemistry, carbon cycling, and trophic dynamics (21, 22).

The quantitative understanding and the associated development of mathematical models for the directed movement of microorganisms have been largely limited to chemotaxis, while other forms of taxis have received considerably less attention despite their ecological importance. For chemotaxis, quantitative experiments have led to a comprehensive characterization of the motile response of bacteria to chemical gradients (23, 24), and this knowledge has been distilled into detailed mathematical models (25). Continuum approaches such as the Keller–Segel model (26, 27), and its generalizations (25), have been used extensively to describe the behavior of chemotactic bacterial populations in laboratory experiments. However, although a limited number of models for phototaxis exists (28–31), an assessment of the phototactic response function is lacking. Existing models rely on untested working hypotheses concerning the cell response to light, originating from the scarcity of experimental work linking controlled light conditions to measured organism responses (*SI Discussion*).

Here, we present quantitative experimental observations of the phototactic response of the flagellate alga *Euglena gracilis* to controlled light gradients. *E. gracilis* is a common freshwater

Significance

Many phytoplankton species sense light and move toward or away from it. Such directed movement, called phototaxis, has major ecological implications because it contributes to the largest biomass migration on Earth, diel vertical migration of organisms responsible for roughly one-half of the global photosynthesis. We experimentally studied phototaxis for the flagellate alga *Euglena gracilis* by tracking algal populations over time in accurately controlled light fields. Observations coupled with formal model comparison lead us to propose a generalized receptor law governing phototaxis of phytoplankton. Such a model accurately reproduces experimental patterns resulting from accumulation and dispersion dynamics. Direct applications concern phytoplankton migrations and vertical distribution, bioreactor optimization, and the experimental study of biological invasions in heterogeneous environments.

Author contributions: A.G., F.A., A.M., R.S., and A.R. designed research; A.G. performed research; A.G., A.M., and A.R. analyzed data; and A.G., F.A., A.M., R.S., and A.R. wrote the paper.

The authors declare no conflict of interest.

This article is a PNAS Direct Submission.

Freely available online through the PNAS open access option.

¹To whom correspondence may be addressed. Email: andrea.rinaldo@epfl.ch or andrea.giometto@epfl.ch.

This article contains supporting information online at www.pnas.org/lookup/suppl/doi:10.1073/pnas.1422922112/-DCSupplemental.

phytoplankton species that swims via an anterior flagellum and uses a paraflagellar body and red stigma (a red eyespot) (32) to respond to light gradients. *E. gracilis* has been used extensively as a model organism in both the ecological (33, 34) and the eco-physiological literature (35, 36) and has been used as a candidate species for technological applications such as photobioreactors (37) and micropellers (38, 39). We use the experimental results to identify a mathematical model for phototaxis. We find that a Keller–Segel-type model (26, 27) accurately describes cell accumulation patterns at all light intensities tested and that the light sensitivity of *E. gracilis* is described by a generalized receptor law (25, 40), a nonlinear function of light intensity that displays a maximum at the light intensity at which cells preferentially accumulate.

Results

We performed laboratory experiments with *E. gracilis* to track the response of algal populations to imposed light conditions. Experiments were conducted in linear channels (5 mm wide \times 3 mm high \times 2 m long) filled with cells ($2,100 \pm 200$ cells·mL⁻¹) suspended in nutrient medium (Fig. 1 and *Materials and Methods*). Light conditions were controlled by light-emitting diodes (LEDs), illuminating the channels from below and operated via Arduino Uno boards (Fig. 1 and *Materials and Methods*). We measured cell distributions in response to localized light sources of different intensity and wavelength λ in the blue ($\lambda = 469$ nm) and red ($\lambda = 627$ nm) regions of the visible spectrum. We measured the light intensity profile $I(x) = I_0 i(x)$ [we set $i(0) = 1$; Fig. S1; units are retained in I_0] in the linear channels (*Materials and Methods*) and we programmed the LEDs to produce the following peak intensities within the channel, at $x = 0$ cm (above the LED): $I_0 = 0.8, 2.3, 5.2, 7.8, 10.4, 20.8, 31.3$ W·m⁻² for $\lambda = 469$ nm and $I_0 = 2.6, 4.7, 10.9, 16.7$ W·m⁻² for $\lambda = 627$ nm. The light profile $i(x)$ was determined by the experimental setting geometry and was invariant for all values of I_0 .

Stationary *E. gracilis* accumulation patterns in blue light are shown in Fig. 2 A–G. Fig. 2 shows that by increasing the peak light intensity I_0 from $I_0 = 0.8$ W·m⁻² to $I_0 = 5.2$ W·m⁻², cell density peaks increase in magnitude (shown are the density profiles normalized by the value at the boundary) and occur in correspondence to the peak in light intensity ($x = 0$ cm). Then, for larger values of I_0 , cell density peaks are approximately constant in magnitude, but shift to the left and right of the source. Cell accumulation was maximum at the light intensity $I \simeq I_m = 5.5$ W·m⁻² (Fig. 2 A–G; $\lambda = 496$ nm; I_m is calculated using the model proposed in the following paragraphs). Light intensities higher than I_m elicited negative phototaxis (directed movement away from the light source), indicating a biphasic response to light (Fig. 2 E–G). Such biphasic responses are common in phototaxis, because they allow cells to increase their photosynthetic activity by migrating toward light while preventing damage to the photosynthetic apparatus and cell pigments at excessive light intensities (42, 43). Our experiments showed clearly no response to red light (Fig. 2 H and I), in line with the reported weak absorption of the *E. gracilis*' eyespot at these wavelengths (44). Red light experiments thus serve as a control that allows us to exclude that the observed cell accumulations toward blue light were due to factors other than phototaxis.

We measured the formation of cell density peaks in time (Fig. 3 A–C), starting from a homogeneous suspension of cells (Fig. 3A), in the presence of a light source of peak intensity $I_0 = 5.2$ W·m⁻² at $x = 0$ cm. Then, we measured the relaxation of the stationary density peaks after the removal of light (Fig. 3 D–F). This allowed us to quantify robustly the cell diffusion coefficient, D , due to the random component of the *E. gracilis* motility (45), by fitting the decay rate of the spectral log-amplitudes $\log|\hat{\rho}(k, t)|$ to the square of the wave number (Fig. 3 G and H and *SI Materials and Methods*). The estimate $D = 0.13 \pm 0.04$ mm²·s⁻¹ is obtained (the SE represents the variability across the first three discrete Fourier transform modes).

The experimental results allowed us to derive a model of phototaxis in *E. gracilis*. We used a Keller–Segel framework, which consists of an advection-diffusion equation for the cell density $\rho(x, t)$ (25) (neglecting cell division owing to the short duration of the experiments):

$$\frac{\partial \rho}{\partial t}(x, t) = \frac{\partial}{\partial x} \left[D \frac{\partial \rho}{\partial x}(x, t) - \frac{d\phi}{dx}[I(x)]\rho(x, t) \right], \quad [1]$$

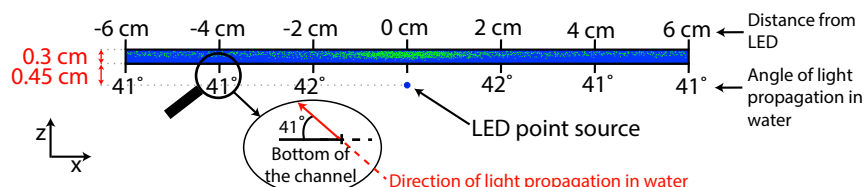
where $v_p = d\phi/dx$ is the drift velocity or “phototactic velocity” of the population in the direction of the light gradient. The phototactic velocity was written as the derivative of a phototactic potential, ϕ , which is solely a function of the light intensity $I(x)$ (25). Such reformulation of the Keller–Segel model allows to express the stationary density distribution as a function of $I(x)$. The steady-state accumulation of cells that satisfies Eq. 1, computed over the spatial extent of the imaging window ($-L \leq x \leq L$; $L = 6.25$ cm), is as follows:

$$\bar{\rho}(x) = \frac{\rho(x)}{\rho(-L)} = \exp \left[\frac{\phi[I(x)]}{D} \right], \quad [2]$$

where $\bar{\rho}(x)$ is the normalized cell density appropriate for comparison with experimental observations. Note that, in general, the exponent should be $\phi[I(x)] - \phi[I(-L)]$, but because ϕ is defined only up to an additive constant we set $\phi[I(-L)] = 0$. Thus, ϕ is set to zero for $I = 0$ (Fig. 4B).

The stationary cell density distributions under blue light (Fig. 2 A–G) together with the measured light intensity profiles (Fig. 4A) were used to derive the phototactic potential $\phi(I)$ from the data. First, we tested the ability of the Keller–Segel model (Eq. 1) to capture the observed phototactic responses in different light regimes. Fig. 4B (*Inset*) shows that the mean cell density profiles $\bar{\rho}(x)$ collapse on the same curve when plotted together as functions of the light intensity (via Eq. 2), thus supporting the applicability of Eq. 1 and the computation of ϕ via Eq. 2, that is, $\phi(I) = D \log \bar{\rho}[x(I)]$. Second, we determined the functional form of the phototactic potential $\phi(I)$. We compared 18 functional forms for $\phi(I)$ using an information-theoretic criterion (46) (*Materials and Methods*). A comparative review of earlier models for phototaxis is provided in *SI Discussion*. The functional forms were chosen by combining monotonically increasing functions of the stimulus I often used to describe sensing, particularly in chemotaxis (25), with monotonically decreasing functions of I ,

Fig. 1. Sketch of the experimental setup. A LED point source (not to scale) was placed below the linear channels. Individuals of *E. gracilis* (green dots; not to scale) accumulated in the presence of light through phototaxis. Shown are distances from the LED and angles of light propagation in water, computed using Snell's law. The light direction component orthogonal to the channel was disregarded here, because the cells' movement dynamics in the vertical direction was dominated by gravitaxis (41), which resulted in the accumulation of cells at the top of the channel (*SI Materials and Methods* and Fig. S6).



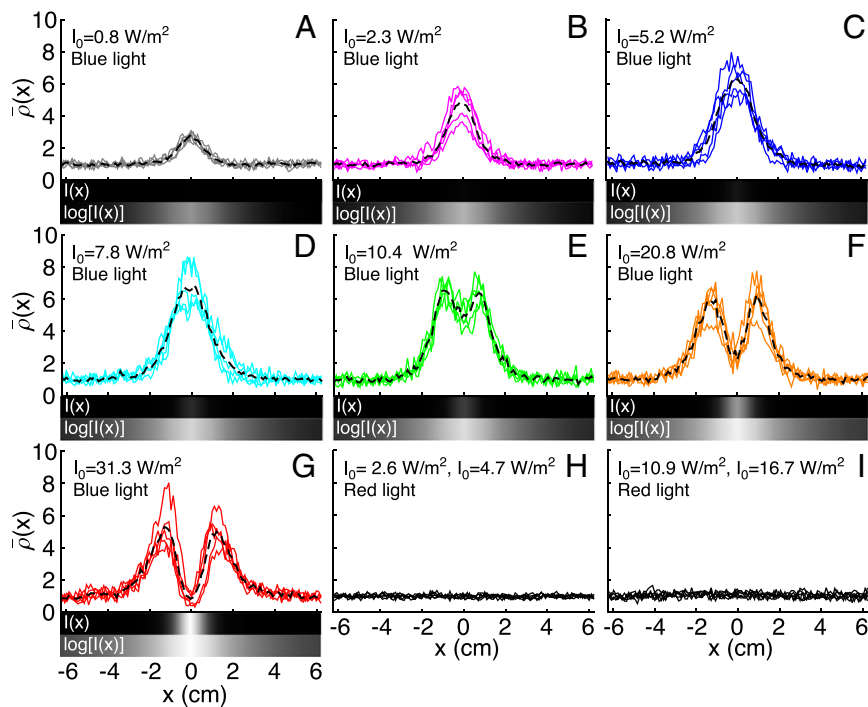


Fig. 2. Phototaxis of *E. gracilis* toward blue and red light of different intensities. Shown are normalized stationary cell density profiles $\bar{\rho}(x)$ around a light source located at $x=0$ cm for various peak intensities I_0 in the blue (A–G; $\lambda=469$ nm) and red (H and I; $\lambda=627$ nm) regions of the visible spectrum. The colored curves in A–G are the experimental cell density distributions (five replicates for each value of I_0), and the dashed black lines denote the mean. The grayscale bars below A–G show the imposed blue light intensity profiles $I(x)$, where the gray level scales linearly (upper bar) or logarithmically (lower bar) with I ; white corresponds to $I=31 \text{ W}\cdot\text{m}^{-2}$ and black to $I=0.001 \text{ W}\cdot\text{m}^{-2}$. Positive phototaxis (directed movement toward the light source) is observed with blue light up to $I \simeq I_m = 5.5 \text{ W}\cdot\text{m}^{-2}$, which is the value of light intensity that causes the highest attraction of algae compared with both lower and higher values (E–G) of I . For $I > I_m$, negative phototaxis (directed movement away from the light source) is observed. No phototactic behavior is discernible with red light (H and I) (three replicates for each value of I_0).

accounting for the photophobic behavior shown experimentally at high light intensity.

By fitting each of the above models (Table S1 and Figs. S2 and S3) to the phototactic potential derived from the data (Fig. 4B), and by using the Akaike Information Criterion (AIC) (46) to formally quantify their relative performance in simulating the experimental patterns discounting the number of parameters, we conclude that our proposed generalization of the receptor law modified to account for the photophobic behavior shown at high light intensities reads as follows:

$$\phi(I) = aI \frac{I_c - I}{I_r + I} \quad [3]$$

where $a = (1.4 \pm 0.04) \cdot 10^{-8} \text{ m}^4 \cdot \text{W}^{-1} \cdot \text{s}^{-1}$, $I_r = 1.7 \pm 0.1 \text{ W}\cdot\text{m}^{-2}$, and $I_c = 28.0 \pm 0.3 \text{ W}\cdot\text{m}^{-2}$ (SEs are calculated via nonlinear least-squares fitting). The phototactic potential displays a maximum ($\phi = 1.8 \text{ mm}^2/\text{s}$) at $I_m = 5.5 \text{ W}\cdot\text{m}^{-2}$ (Fig. 4B), the light intensity value that separates the positive and negative phototaxis regimes, and is equal to zero at $I_c = 28.0 \text{ W}\cdot\text{m}^{-2}$. The phototactic velocity $v_p = d\phi/dx$ corresponding to Eq. 3 in our experimental light conditions is shown in Fig. S4. Eq. 3 yields the best model for phototaxis in *E. gracilis* in reproducing the measured stationary cell density profiles (Fig. 4C and D).

The proposed phototaxis model, although derived from stationary distributions, correctly captures also the temporal dynamics of phototaxis (red dashed lines in Fig. 3A–F), that is, the formation of density peaks in the presence of light and their subsequent dissipation following light removal (note that Eq. 1 reduces to the diffusion equation in the absence of light stimuli). Small deviations from the model prediction during cell accumulation (Fig. 3A–C) are observed. They are possibly due to the repeated transfers of the channel from the illumination setup to the stereomicroscope for algal density measurements.

Discussion

To compare our experimental setup with natural environments, we note that integrating the ASTM G-173 reference terrestrial

solar spectral irradiance (47) in a wavelength window of 10 nm centered at $\lambda = 469$ nm (10 nm is the typical width of emission for our LEDs; Materials and Methods) gives a typical irradiance of $\sim 13 \text{ W}\cdot\text{m}^{-2}$ at sea level. Wavelengths in the blue region of the visible spectrum are among the most transmitted in natural aquatic habitats (11, 48) and penetrate the farthest in the water column, whereas red light is the most attenuated. Thus, the range of light intensities and wavelengths used in the experiments is typical of natural conditions, suggesting that our experimental and theoretical results may have implications for the behavior of phytoplankton in natural environments.

The response of cells to light of different intensities, here expressed in terms of the phototactic potential $\phi(I)$, was inferred from measured stationary cell density profiles. However, the model was shown to capture also the temporal dynamics of cell accumulation around a light source and the diffusive relaxation following light removal. Interestingly, the proposed choice of receptor law, subsumed by $\phi(I)$, includes both positive and negative phototaxis within the same mathematical framework. Although we cannot exclude that phototactic microorganisms may in general sense both the intensity and directionality of light, our model based on intensity alone outperforms other models including both intensity and directionality of light propagation (SI Discussion, Fig. S5, and Tables S1–S5), at least for our experimental setting.

Our experimental approach to phototaxis provides a template for the study of ecological processes in shifting and fluctuating resource availability. In fact, the convenient use of programmable LEDs allows one to create microbial microcosms in which light conditions can be accurately controlled to generate a boundless variety of spatiotemporal patterns of environmental stochasticity, affecting both the growth and the movement behavior of cells. Hence, the study system developed here is suggested to be a promising candidate for quantitative microcosm experiments on biological invasions along ecological corridors, range expansions, and source-sink dynamics under environmental noise (49–52).

All things considered, we suggest that the literature lacked an experimentally tested mathematical framework comprising a measure of the phototactic response function of phototactic populations. This work is thus suggested to provide the blueprint for

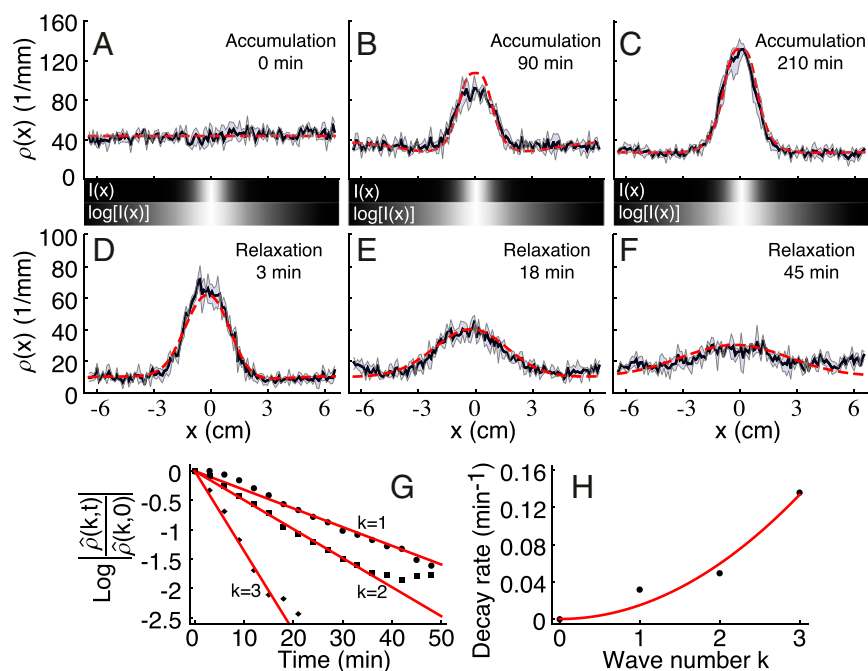


Fig. 3. Temporal dynamics of accumulation around a light source at $x=0$ cm (A–C) and relaxation of cell density peaks upon removal of light (D–H). (A–F) Experimental cell density profiles at different times. The shaded gray area is delimited by the maximum and minimum cell densities of three replicate experiments and the black line denotes the mean. The red dashed line shows the theoretical prediction, Eq. 1, using the experimentally determined $\phi(I)$ and $I(x)$ (Fig. 4 A and B) and D (Table 1) determined experimentally from the relaxation of density peaks (D–H). Density profiles are renormalized to display the same mean abundance. The grayscale bars below A–C show the light intensity profile imposed during the accumulation; the gray level scales linearly (upper panels) or logarithmically (lower panels) with the intensity I , with white corresponding to $I=5.2$ $\text{W}\cdot\text{m}^{-2}$ and black to $I=0.001$ $\text{W}\cdot\text{m}^{-2}$. The temporal decay of Fourier modes (G) during the relaxation of density peaks (D–F) is exponential $|\log[\hat{\rho}(k, t)/\hat{\rho}(k, 0)]| = -Dk^2t$; data in black and linear fit in red, and the decay rate is a quadratic function of the wave number k (H; data in black and parabolic fit in red), proving the diffusive behavior in the absence of light gradients.

the characterization of the collective response of phytoplankton to light availability and its migration strategies in aquatic ecosystems. Identification of the light intensity regime where positive and negative phototaxis occur pinpoints the regions of the water column where phototactic effects affect the vertical distribution of phytoplankton. Currently, models of phytoplankton growth in contrasting gradients of light and nutrients aimed at reproducing the vertical distribution of phytoplankton, either ignore phototaxis (53) or rely on untested assumptions for the phototactic advection velocity $v_p = d\phi[I(x)]/dx$ (54, 55). The identification of the functional form for $\phi(I)$ provided here can be used directly to integrate realistic predictions for the phytoplankton vertical distribution, which is relevant for global biogeochemical cycles, diversity and coexistence of plankton species, and ecosystem functioning (56, 57). The interspecific variability of the optimal light intensity [defined by $d\phi(I)/dI = 0$] and nutrient requirements have been argued (58) to translate into a sectoring of the water column into separate niches, allowing the coexistence of competitive species.

The mathematical framework derived here may also serve to improve the design of algal bioreactors. Phototaxis of swimming algae, sometimes in combination with other directional behaviors such as gravitaxis (the directed swimming in response to gravity) and gyrotaxis (gravitaxis in the presence of ambient velocity gradients), is speculated to have implications for the design of algal

photobioreactors. The phototaxis model proposed here (Eq. 1) may be used directly to refine existing models for photo-gyrotactic (31) and photo-gyro-gravitactic (59) bioconvection, which currently rely on educated guesses for the phototactic advection term. Our model may be applied to identify optimal designs for cell accumulation far from the reactor surface to avoid biofouling and to achieve enhanced harvesting, a strategy that has been investigated experimentally (37). For example, the fact that the phototactic potential ϕ is much steeper for light intensities above $I_m = 5.5$ $\text{W}\cdot\text{m}^{-2}$ than below such value, and hence the phototactic velocity is larger for $I > I_m$, suggests that the exploitation of negative phototaxis might be a more effective strategy than the use of positive phototaxis to achieve optimal harvesting.

Algae are also increasingly used in microbiomachine research, for example as micropellers for the transport of colloidal cargo (38, 39), where light can be used as the external driver of the motion. Although this research is yet to translate into practice, it represents an exciting avenue to harness microbial motility for controlled microscale applications, and phototaxis represents one of the most controllable processes because of the ease of accurately imposing and rapidly modulating external light gradients. The algorithms that are currently used to control such microbiomachines are mostly empirical, and our model may indeed serve to render machine control more robust and accurate. Much attention is currently dedicated to understanding the swimming behavior in these artificial environments (60) and our characterization of collective phototactic dynamics might be exploited to optimize existing technological applications or design new ones.

In the broadest sense, our work provides a blueprint for obtaining robust, quantitative data on directed cell motility, and our method is straightforward to extend to diverse photosynthetic species of plankton, enabling a better understanding of how these important organisms move and live in natural or man-made heterogeneous environments.

Materials and Methods

Algal Culture. The species used in the experiments, *E. gracilis*, was purchased from Carolina Biological Supply and maintained in a nutrient medium (33, 34) composed of sterilized spring water and Protozoan Pellets (Carolina Biological Supply) at a density of 0.45 $\text{g}\cdot\text{L}^{-1}$, filtered through a 0.2 - μm filter. Algal cultures were initialized 2 wk before the start of the experiment and

Table 1. Parameters describing the phototactic response and movement dynamics of *E. gracilis*

Parameter	Value
Phototactic response	
a	$(1.4 \pm 0.04) \cdot 10^{-8}$ $\text{m}^4\cdot\text{W}^{-1}\cdot\text{s}^{-1}$
I_r	1.7 ± 0.1 $\text{W}\cdot\text{m}^{-2}$
I_c	28.0 ± 0.3 $\text{W}\cdot\text{m}^{-2}$
Movement dynamics	
D	0.13 ± 0.04 $\text{mm}^2\cdot\text{s}^{-1}$

Values shown are mean \pm SE. The parameters a , I_r , and I_c define the phototactic potential ϕ . The diffusion coefficient D was estimated via the relaxation of density peaks (Fig. 3 D–H). See *SI Materials and Methods* and *Figs. S7* and *S8* for measurements of the movement dynamics of individual cells.

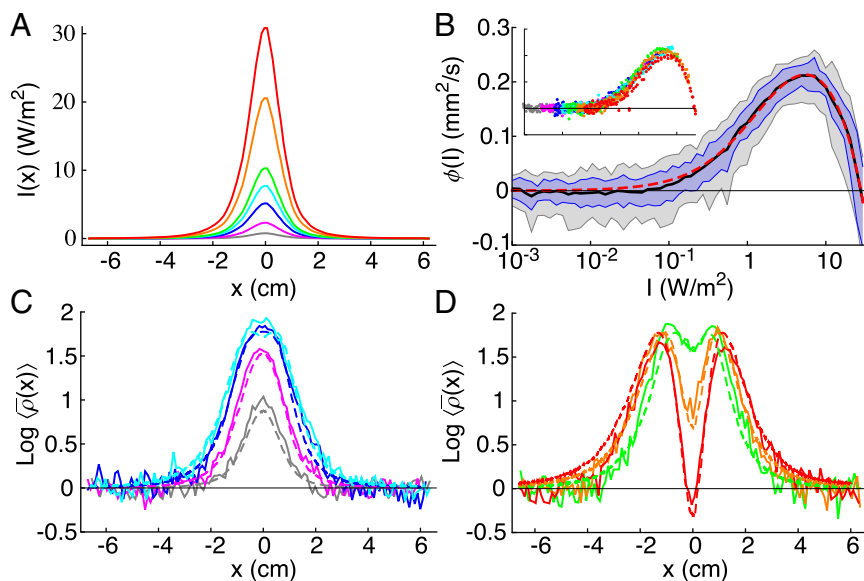


Fig. 4. Computation of the phototactic potential $\phi(I)$. (A) Light intensity profiles for different peak intensities I_0 . (B) Phototactic potential $\phi(I)$ computed from Eq. 2 via inversion of the light intensity profile $I(x)$ (A). The solid black line is the mean value of $\phi(I)$ over the stationary density profiles for the various I_0 , whereas the blue and gray regions represent the 68% and 95% confidence intervals, respectively. The dashed red line is the best fit of the phototactic potential predicted by the modified receptor law, Eq. 3. (Inset) The phototactic potential calculated from each of the stationary density profiles (colored by light intensity regime; see A and Fig. 2 A–G) at different I_0 collapse on the same curve [displayed on the y axis is the quantity $\phi(I) = D \log(\bar{\rho}(x))$, where the mean is over the five replicates with same I_0], proving the applicability of Eq. 1. Axes labels and ticks are as in the enclosing figure. (C and D) Mean cell density profiles measured at steady state (solid lines) and predicted from Eq. 2 (dashed lines), color-coded according to the light intensity regime (see A and Fig. 2 A–G).

kept at a constant temperature of 22 ° C under constant LED light at $\lambda = 469$ nm. *E. gracilis* individuals have a typical linear size of 14 μ m (34), and the duplication time is ~ 20 h (33); thus, reproduction can be neglected in our experiments.

Linear Landscapes. The linear landscapes (Fig. 1) used in the experiments were channels drilled on a Plexiglas sheet (61). A second Plexiglas sheet was used as a cover, and a gasket prevented water spillage. Before the introduction of the algal culture to the linear landscapes, the Plexiglas sheets were sterilized with a 70% (vol/vol) ethanol solution, and the gaskets were autoclaved.

Light Sources and Light Intensity Profile. A linear array of LEDs was developed to control the light intensity profile along the linear landscapes. LEDs were placed below the linear channels (Fig. 1). RGB (red, green, blue) LED strips (LED: SMD 5050; chip: WS2801 IC) were controlled via Arduino Uno boards. The LED strips consisted of individually addressable LEDs separated by a distance of 3.12 cm. The light intensity for the B (blue) and R (red) color channels (wavelengths of 463–475 and 619–635 nm, respectively) could be controlled. We measured the total radiant flux emitted by LEDs at the different intensities and wavelengths used with a calibrated photodiode. The relative light intensity profiles, with the LEDs set at the different intensities used, was measured by placing a white paper sheet in the linear channels and measuring the irradiance on the sheet with a digital camera operated in grayscale at fixed aperture, exposure, and distance from the LED. This relative measure of light intensity was converted to absolute values via the total radiant flux measured. In the experiments, periodic light intensity profiles were established with one LED switched on every 12.5 cm. The experimentally measured relative light intensity profile $i(x)$ was found to be well described by the functional form $i(x) = c_0/(x^2 + c_1^2)^2$ (Fig. S1).

Density Measurements. Density profiles were measured at the center of the linear landscape across one entire period of the light intensity profile. Density estimates were obtained by placing the linear landscape under the objective of a stereomicroscope (Olympus SZX16), taking pictures (with the camera Olympus DC72), and counting individuals through image analysis as in ref. 61. Stationary density profiles were measured after 210 min from the introduction of cells in the landscape. In the phototactic accumulation measurements, the landscapes were moved from the support holding the LEDs used for experimentation to

the stage of the stereomicroscope just before performing the density measurement. Imaging of the 12-cm imaging window took less than 30 s. Thereby, we assume that no significant relaxation or redistribution of algae occurred during the measurement time. To measure the relaxation of density peaks, the linear landscapes were placed on the stage of the stereomicroscope and the white LED light for microscopy was switched on solely during the measurement time. Landscapes were covered with black cardboard and kept in a dark room to avoid external light during all of the experiments, except during imaging.

Phototactic Potential. To investigate the suitable functional form of the phototactic potential, we combined a set of models that have been used to describe sensing in chemotaxis (25) with a set of monotonically decreasing functions aimed at reproducing the photophobic behavior at high light intensity. The resulting functional forms were formally compared via the AIC to probe their performance in reproducing our laboratory data. The first set, which consists of monotonically increasing functions of light intensity, is as follows: $\phi_1(I) = aI$, $\phi_2(I) = aI/(1 + bI)$, and $\phi_3(I) = a \log(1 + bI)$. These functional forms have been used to describe chemotactic responses (25). The second set consists of monotonically decreasing functions of light intensity I , specifically: $\phi_A(I) = -\log(1 + cI)$, $\phi_B(I) = -c\sqrt{I}$, and $\phi_C(I) = -cI$, respectively. The functional forms in the second set were chosen to allow $\lim_{I \rightarrow \infty} \phi = -\infty$ (some of the combinations do not satisfy this limiting behavior; e.g., Fig. S3). In fact, experimental observations show that $\bar{\rho}(x) = 0$ if the light intensity in x grows too large. In such case, $\phi(x) = D \log(\bar{\rho}(x)) = -\infty$. Models from the first set were combined with models from the second set both in additive and multiplicative fashions (SI Materials and Methods). We fitted all models to the data (Figs. S2 and S3) and computed the corresponding AIC values (Table S1). The best model according to the AIC is $\phi_{2c} = aI(1 - cI)/(1 + bI)$.

ACKNOWLEDGMENTS. We thank Enrico Bertuzzo, Francesco Carrara, and Lorenzo Mari for discussions and comments, and Antonino Castiglia, Nicolas Grandjean, and Marco Malinverni for support in the light intensity measurement. We gratefully acknowledge the support provided by Swiss Federal Institute of Aquatic Science and Technology (Eawag) discretionary funds; the European Research Council advanced grant program through the project “River Networks as Ecological Corridors for Biodiversity, Populations and Waterborne Disease” (RINEC-227612); and Swiss National Science Foundation Projects 200021_124930/1, 200021_157174, and 31003A_135622. R.S. acknowledges support through a Gordon and Betty Moore Marine Microbial Initiative Investigator Award (GBMF3783).

1. Hazelbauer GL, Berg HC, Matsumura P (1993) Bacterial motility and signal transduction. *Cell* 73(1):15–22.
2. Stocker R (2012) Marine microbes see a sea of gradients. *Science* 338(6107):628–633.
3. Laughlin S (1981) A simple coding procedure enhances a neuron's information capacity. *Z Naturforsch C* 36(9–10):910–912.
4. Kussell E, Leibler S (2005) Phenotypic diversity, population growth, and information in fluctuating environments. *Science* 309(5743):2075–2078.
5. Celani A, Vergassola M (2010) Bacterial strategies for chemotaxis response. *Proc Natl Acad Sci USA* 107(4):1391–1396.

6. Mesibov R, Ordal GW, Adler J (1973) The range of attractant concentrations for bacterial chemotaxis and the threshold and size of response over this range. Weber law and related phenomena. *J Gen Physiol* 62(2):203–223.
7. Shoval O, et al. (2010) Fold-change detection and scalar symmetry of sensory input fields. *Proc Natl Acad Sci USA* 107(36):15995–16000.
8. Lazova MD, Ahmed T, Bellomo D, Stocker R, Shimizu TS (2011) Response rescaling in bacterial chemotaxis. *Proc Natl Acad Sci USA* 108(33):13870–13875.
9. Levin SA (1994) Patchiness in marine and terrestrial systems: From individuals to populations. *Philos Trans R Soc Lond B Biol Sci* 343(1303):99–103.

10. Azam F (1998) Microbial control of oceanic carbon flux: The plot thickens. *Science* 280(5364):694–696.
11. Ragni M, Ribera D'Alcala M (2004) Light as an information carrier underwater. *J Plankton Res* 26(4):433–443.
12. Bhaya D (2004) Light matters: Phototaxis and signal transduction in unicellular cyanobacteria. *Mol Microbiol* 53(3):745–754.
13. Jékely G, et al. (2008) Mechanism of phototaxis in marine zooplankton. *Nature* 456(7220):395–399.
14. Hays GC (2003) A review of the adaptive significance and ecosystem consequences of zooplankton diel vertical migrations. *Hydrobiologia* 503(1-3):163–170.
15. Ringelberg J, Flik BJB (1994) Increased phototaxis in the field leads to enhanced diel vertical migration. *Limnol Oceanogr* 39(8):1855–1864.
16. Kingston MB (1999) Effect of light on vertical migration and photosynthesis of *Euglena proxima* (Euglenophyta). *J Phycol* 35(2):245–253.
17. Smayda TJ (1997) Harmful algal blooms: Their ecophysiology and general relevance to phytoplankton blooms in the sea. *Limnol Oceanogr* 42(5 Pt 2):1137–1153.
18. Field CB, Behrenfeld MJ, Randerson JT, Falkowski P (1998) Primary production of the biosphere: Integrating terrestrial and oceanic components. *Science* 281(5374):237–240.
19. Behrenfeld MJ, et al. (2006) Climate-driven trends in contemporary ocean productivity. *Nature* 444(7120):752–755.
20. Chassot E, et al. (2010) Global marine primary production constrains fisheries catches. *Ecol Lett* 13(4):495–505.
21. Falkowski PG, Barber RT, Smetacek V (1998) Biogeochemical controls and feedbacks on ocean primary production. *Science* 281(5374):200–207.
22. Boyce DG, Lewis MR, Worm B (2010) Global phytoplankton decline over the past century. *Nature* 466(7306):591–596.
23. Adler J, Hazelbauer GL, Dahl MM (1973) Chemotaxis toward sugars in *Escherichia coli*. *J Bacteriol* 115(3):824–847.
24. Barbara GM, Mitchell JG (2003) Bacterial tracking of motile algae. *FEMS Microbiol Ecol* 44(1):79–87.
25. Tindall MJ, Maini PK, Porter SL, Armitage JP (2008) Overview of mathematical approaches used to model bacterial chemotaxis II: Bacterial populations. *Bull Math Biol* 70(6):1570–1607.
26. Keller EF, Segel LA (1970) Initiation of slime mold aggregation viewed as an instability. *J Theor Biol* 26(3):399–415.
27. Keller EF, Segel LA (1971) Model for chemotaxis. *J Theor Biol* 30(2):225–234.
28. Burkart U, Häder DP (1980) Phototactic attraction in light trap experiments: A mathematical model. *J Math Biol* 10(3):257–269.
29. Torney C, Neufeld Z (2008) Phototactic clustering of swimming microorganisms in a turbulent velocity field. *Phys Rev Lett* 101(7):078105.
30. Vincent RV, Hill NA (1996) Bioconvection in a suspension of phototactic algae. *J Fluid Mech* 327:343–371.
31. Williams CR, Bees MA (2011) Photo-gyrotactic bioconvection. *J Fluid Mech* 678:41–86.
32. Jékely G (2009) Evolution of phototaxis. *Philos Trans R Soc Lond B Biol Sci* 364(1531):2795–2808.
33. Altermatt F, et al. (2015) Big answers from small worlds: A user's guide for protist microcosms as a model system in ecology and evolution. *Methods Ecol Evol* 6(2):218–231.
34. Giometto A, Altermatt F, Carrara F, Maritan A, Rinaldo A (2013) Scaling body size fluctuations. *Proc Natl Acad Sci USA* 110(12):4646–4650.
35. Wolken J (1961) *Euglena: An Experimental Organism for Biochemical and Biophysical Studies* (Rutgers Univ Press, New Brunswick, NJ).
36. Vallee BL, Falchuk KH (1993) The biochemical basis of zinc physiology. *Physiol Rev* 73(1):79–118.
37. Ooka H, Ishii T, Hashimoto K, Nakamura R (2014) Light-induced cell aggregation of *Euglena gracilis* towards economically feasible biofuel production. *R Soc Chem Adv* 4(40):20693–20698.
38. Itoh A (2004) *Euglena* motion control by local illumination. *Bio-mechanisms of Swimming and Flying*, eds Kato N, Ayers J, Morikawa H (Springer, Tokyo), pp 13–26.
39. Itoh A, Tamura W (2008) Object manipulation by a formation-controlled *Euglena* group. *Bio-mechanisms of Swimming and Flying*, eds Kato N, Kamimura S (Springer, Tokyo), pp 41–52.
40. Lapidus IR, Schiller R (1976) Model for the chemotactic response of a bacterial population. *Biophys J* 16(7):779–789.
41. Häder DP, Griebenow K (1988) Orientation of the green flagellate, *Euglena gracilis*, in a vertical column of water. *FEMS Microbiol Ecol* 53(3-4):159–167.
42. Häder DP, Lebert M (1998) The photoreceptor for phototaxis in the photosynthetic flagellate *Euglena gracilis*. *Photochem Photobiol* 68(3):260–265.
43. Lebert M, Porst M, Richter P, Häder DP (1999) Physical characterization of gravitaxis in *Euglena gracilis*. *J Plant Physiol* 155(3):338–343.
44. Strother GK, Wolken JJ (1960) Microspectrophotometry of *Euglena* chloroplast and eyespot. *Nature* 188(4750):601–602.
45. Ahmed T, Stocker R (2008) Experimental verification of the behavioral foundation of bacterial transport parameters using microfluidics. *Biophys J* 95(9):4481–4493.
46. Burnham KP, Anderson DR (2002) *Model Selection and Multimodel Inference: A Practical Information-Theoretic Approach* (Springer, New York), 2nd Ed.
47. ASTM International (2008) Standard tables for reference solar spectral irradiances, direct normal and hemispherical on 37° tilted surface. ASTM Standard G173 (ASTM International, West Conshohocken, PA).
48. Jeffrey S (1984) Responses of unicellular marine plants to natural blue-green light environments. *Proceedings in Life Sciences*, ed Senger H (Springer, Berlin), pp 497–508.
49. Gonzalez A, Holt RD (2002) The inflationary effects of environmental fluctuations in source-sink systems. *Proc Natl Acad Sci USA* 99(23):14872–14877.
50. Bertuzzo E, et al. (2007) River networks and ecological corridors: Reactive transport on fractals, migration fronts, hydrochory. *Water Resour Res* 43(4):W04419.
51. Rodriguez-Iturbe I, et al. (2009) River networks as ecological corridors: A complex systems perspective for integrating hydrologic, geomorphologic and ecologic dynamics. *Water Resour Res* 45(1):W01413.
52. Méndez V, Llopis I, Campos D, Horsthemke W (2011) Effect of environmental fluctuations on invasion fronts. *J Theor Biol* 281(1):31–38.
53. Greenwood J, Craig P (2014) A simple numerical model for predicting vertical distribution of phytoplankton on the continental shelf. *Ecol Modell* 273:165–172.
54. Klausmeier CA, Litchman E (2001) Algal games: The vertical distribution of phytoplankton in poorly mixed water columns. *Limnol Oceanogr* 46(8):1998–2007.
55. Mellard JP, Yoshiyama K, Litchman E, Klausmeier CA (2011) The vertical distribution of phytoplankton in stratified water columns. *J Theor Biol* 269(1):16–30.
56. Steele JH, Yentsch CS (1960) The vertical distribution of chlorophyll. *J Mar Biol Assoc UK* 39(2):217–226.
57. Lampert W, McCauley E, Manly BFF (2003) Trade-offs in the vertical distribution of zooplankton: Ideal free distribution with costs? *Proc Biol Sci* 270(1516):765–773.
58. Yoshiyama K, Mellard JP, Litchman E, Klausmeier CA (2009) Phytoplankton competition for nutrients and light in a stratified water column. *Am Nat* 174(2):190–203.
59. Williams CR, Bees MA (2011) A tale of three taxes: Photo-gyro-gravitactic bioconvection. *J Exp Biol* 214(Pt 14):2398–2408.
60. García X, Rafāi S, Peyla P (2013) Light control of the flow of phototactic microswimmer suspensions. *Phys Rev Lett* 110(13):138106.
61. Giometto A, Rinaldo A, Carrara F, Altermatt F (2014) Emerging predictable features of replicated biological invasion fronts. *Proc Natl Acad Sci USA* 111(1):297–301.

Supporting Information

Giometto et al. 10.1073/pnas.1422922112

SI Materials and Methods

Density Estimates and Video Recording. Border effects were neglected because the density measurements were always performed at the center of the landscape, which had a total length (2 m) that was much larger than the length of one period of the light intensity profile (12.5 cm). To reconstruct the trajectories, videos were recorded with a stereomicroscope (*Materials and Methods*) and particle tracking was performed automatically with the MOSAIC (1) plug-in for ImageJ under homogeneous light conditions and manually with the MTrackJ plug-in for ImageJ in the presence of nonuniform light (automatic tracking was not possible in the nonuniform light setup because of the low quality of pictures, due to the use of only one LED light for the microscopy).

Vertical Distribution of Cells. Cells were observed to accumulate on one layer at the top of the channel, both in the presence and in the absence of light. This vertical distribution of cells is not due to phototaxis, but is caused by a phenomenon known as negative gravitaxis, that is, the movement of *Euglena gracilis* in the direction opposed to gravity (2). In fact, the distribution of algae is skewed toward the top of the channel regardless of the positioning of the LED above or below the linear landscapes, as shown in Fig. S6. Such skewed distribution of algae in the vertical direction bears no implications for the validity of our results once the density distribution data are integrated in the vertical direction.

Population Estimate of the Diffusion Coefficient. The population estimate of the diffusion coefficient D (Table 1) was based on the relaxation of density peaks (Fig. 3 *D–H*). Density profiles at different times were Fourier-transformed in space and the decay of their log amplitudes $\log[|\hat{\rho}(k, t)|/|\hat{\rho}(k, 0)|]$ in time was fitted to the linear model $-Dk^2t$ for $k = 1, 2, 3$ (Fig. 3*G*) in all experimental replicates. The mean exponential decay rate as a function of k across replicas was then fitted to the parabola Dk^2 (Fig. 3*H*) to estimate D .

Phototactic Potential. To investigate the functional form of the phototactic potential, we combined a set of models that have been used to describe sensing in chemotaxis (3) with a set of monotonically decreasing functions aimed at reproducing the photophobic behavior at high light intensity. The resulting functional forms were compared via the Akaike Information Criterion (AIC) to compare their performance in predicting the data. The first set of models, which consists of monotonically increasing functions of light intensity, is as follows:

$$\begin{aligned} \cdot \phi_1(I) &= aI, \\ \cdot \phi_2(I) &= a \frac{I}{1 + bI}, \\ \cdot \phi_3(I) &= a \log(1 + bI). \end{aligned}$$

These models have been used extensively to describe chemotactic responses (3). The second set of models consists of monotonically decreasing functions of light intensity I :

$$\begin{aligned} \cdot \phi_A(I) &= -\log(1 + cI), \\ \cdot \phi_B(I) &= -c\sqrt{I}, \\ \cdot \phi_C(I) &= -cI. \end{aligned}$$

The functional forms in the second set were chosen to allow $\lim_{I \rightarrow \infty} \phi = -\infty$ (some of the combinations do not satisfy this limiting behavior, resulting in poor fits; e.g., Fig. S3). In fact, experimental observation show that $\bar{\rho}(x) = 0$ if the light intensity in x is too high. In such situation, $\phi(x) = D \log[\bar{\rho}(x)] = -\infty$. Models from the first set were combined with models from the second set both in a multiplicative (e.g., $\phi_{1A} = \phi_1 \cdot (1 + \phi_A) = aI[1 - \log(1 + cI)]$) and additive [e.g., $\phi_{1A} = \phi_1 + \phi_A = aI - \log(1 + cI)$] fashion. We fitted all models to the data (Figs. S2 and S3) and computed the corresponding AIC values, which are reported in Table S1. The best model according to the AIC is $\phi_{2C} = aI(1 - cI)/(1 + bI)$; all other models have a ΔAIC value (compared with the best model) larger than 7 and are thus unlikely (4). The AIC is unable to distinguish between the additive and multiplicative form of the model combination ϕ_2 and ϕ_C , because the ΔAIC difference between the additive combination, $\phi_{2C} = aI/(1 + bI) - cI$, and the multiplicative one, $\phi_{2C} = aI(1 - cI)/(1 + bI)$, is only $\Delta\text{AIC} = -0.0005$. We thus assumed the combination yielding the smallest AIC index, the multiplicative one, as the best model.

Swimming Trajectories. To characterize the swimming behavior at the single-cell level, we recorded trajectories of individual *E. gracilis* cells (Fig. S7), both in a uniform light field and within a nonuniform one. The statistics of cell motion in uniform light (Fig. S7) are in good agreement with the Ornstein–Uhlenbeck (OU) process (5, 6):

$$\begin{cases} \dot{x} = v \\ \dot{v} = -\gamma v + \sigma \eta(t) \end{cases} \quad [\text{S1}]$$

where x is the (one-dimensional) position of the cell, v is its instantaneous velocity, and $\eta(t)$ is a Gaussian white noise. The diffusive behavior observed at the population level finds confirmation by the analyses at the level of individual cells at much smaller spatial and temporal scales (Fig. S7*C*). In fact, a quantitative agreement between the diffusion coefficients at the two scales is observed. However, no net displacement is observable at the single-cell scale over the duration (60 s) of tracking trajectories recorded in nonuniform light, because the random component of the motion dominates over phototactic drift. A mathematical framework for the motion of individual cells in the presence of nonuniform light fields is proposed in the following section and is used therein to explain the impossibility to observe a net bias toward the source in the experimental trajectories at such timescales. The analysis of individual trajectories that characterizes the typical swimming behavior of cells provides information on the instantaneous speed v and the typical autocorrelation time τ of swimming trajectories. This might be of interest in view of phototactic applications of microorganisms as micropropellers.

Uniform light. We measured 330 trajectories of cells through dark-field microscopy, placing the recording window at the center of the microscope stage to minimize light gradients and thus bias in the direction of motion. We analyzed the recorded trajectories by computing the mean square displacement, mean square velocity, velocity autocorrelation, and velocity distribution along the direction of the channel (Fig. S7). We analyzed the x coordinates of the recorded trajectories, that is, the coordinate of each individual in the direction of the linear landscape, which was also the direction of the light gradient under the nonuniform light conditions. The statistics (Fig. S7) of cells' motion in uniform light are in good agreement with the OU process (5, 6). Specifically, the mean square displacement $\langle \Delta x^2(t) \rangle$, mean square velocity $\langle v^2(t) \rangle$,

and velocity autocorrelation $\langle v(t)v(0) \rangle$ were fitted to their analytical expressions (5):

$$\langle \Delta x^2(t) \rangle_{OU} = \frac{\sigma^2}{\gamma^2} \left[t - \frac{2}{\gamma} (1 - e^{-\gamma t}) + \frac{1}{2\gamma} (1 - e^{-2\gamma t}) \right] + \frac{v_0^2}{\gamma^2} (1 - e^{-\gamma t})^2, \quad [S2]$$

$$\langle v^2(t) \rangle_{OU} = v_0^2 e^{-2\gamma t} + \frac{\sigma^2}{2\gamma} [1 - e^{-2\gamma t}], \quad [S3]$$

$$\langle v(t)v(0) \rangle_{OU} = v_0^2 e^{-\gamma t}. \quad [S4]$$

The quantity γ^{-1} measures the typical timescale of the velocity autocorrelation, whereas σ describes the degree of stochasticity of the motion. The fit was performed simultaneously for the three curves (red lines in Fig. S7), that is, the best fit parameters for γ and σ were those that minimized the χ^2 :

$$\chi^2 = 1/2 \left[\sum_{i=1}^T \left(\langle \Delta x^2(t) \rangle_{data} - \langle \Delta x^2(t) \rangle_{OU} \right)^2 / \sigma_{\langle \Delta x^2(t) \rangle}^2 + \sum_{i=1}^T \left(\langle v^2(t) \rangle_{data} - \langle v^2(t) \rangle_{OU} \right)^2 / \sigma_{\langle v^2(t) \rangle}^2 + \sum_{i=1}^T \left(\langle v(t)v(0) \rangle_{data} - \langle v(t)v(0) \rangle_{OU} \right)^2 / \sigma_{\langle v(t)v(0) \rangle}^2 \right],$$

where σ^2 indicates the SE of the mean in the data. The parameters' errors are given by the square root of the diagonal elements of the Hessian matrix, which is evaluated at the minimum. This fitting procedure provided the estimates $\gamma = 0.077 \pm 0.014 \text{ s}^{-1}$ and $\sigma = 0.032 \pm 0.004 \text{ mm/s}^{3/2}$ (mean \pm SE). The cyan lines in Fig. S7 were obtained by fitting the velocity autocorrelation to its analytical expression Eq. S4 and subsequently fitting σ separately to the mean square displacement via Eq. S2 and to the mean square velocity via Eq. S3. This fitting procedure provided the estimates $\gamma = 0.054 \pm 0.014 \text{ s}^{-1}$ and $\sigma = 0.025 \pm 0.003 \text{ mm/s}^{3/2}$ (mean \pm SE). The diffusive behavior observed at the population level finds additional confirmation at the individual level (at times $t > \gamma^{-1} = \tau$; Fig. S7C), with quantitative agreement between the diffusion coefficients at the two scales [for the trajectories data, $D = \sigma^2 / (2\gamma^2) = 0.09 \pm 0.04 \text{ mm}^2 \cdot \text{s}^{-1}$, where we have used the mean values of γ and σ obtained with the two fitting procedures]. The mean (instantaneous) swimming speed of *E. gracilis* cells was $\bar{v} = 0.10 \pm 0.05 \text{ mm} \cdot \text{s}^{-1}$, mean \pm SE.

Nonuniform light. We measured 130 trajectories of individual organisms that were recorded in the presence of an imposed nonuniform light field (Fig. S8), obtained by placing a LED with $I_0 = 5.2 \text{ W} \cdot \text{m}^{-2}$ at the right border of the imaging window, and found no net displacement toward the light source (Fig. S8B). The mean (instantaneous) swimming speed of *E. gracilis* cells was the same in nonuniform ($\bar{v} = 0.10 \pm 0.04 \text{ mm} \cdot \text{s}^{-1}$; mean \pm SE) and uniform light. The mean phototactic velocity $\bar{v}_p = \langle d\phi/dx \rangle$ in the imaging window (the mean is computed over space) (Eq. 2) is $\bar{v}_p = 0.007 \text{ mm} \cdot \text{s}^{-1}$; therefore, the directionality of swimming $\bar{v}_p/\bar{v} = 0.07$ is very small.

Despite the difficulty of discerning phototaxis at the single-cell level, the good agreement of trajectory statistics with the OU model in uniform light and the observation of accumulation dynamics around light sources at the population level suggest the following Langevin model for the phototaxis of individual cells,

$$\begin{cases} \dot{x} = v \\ \dot{v} = -\gamma v + \sigma \eta(t) + \gamma \frac{d\phi[I(x)]}{dx}, \end{cases} \quad [S5]$$

where x is the (one-dimensional) position of the cell, v is its instantaneous velocity, $\eta(t)$ is a Gaussian white noise, and $\phi[I(x)]$ is the phototactic potential. In the presence of nonuniform light, the term $\gamma d\phi[I(x)]/dx$ in Eq. S5 drives the accumulation of individuals around the light source in the long term. This single-cell model is consistent with the Keller–Segel model at the population scale (Eq. 1) and reduces to the OU model in the absence of external gradients. However, given that we could not discern the biased movement toward the light source at the individual cell level, no direct evidence of the applicability of Eq. S5 is available and further experimentation is required.

To interpret the failure to detect a bias toward the light source, we performed 1,000 integrations of Eq. S5, with initial positions drawn uniformly at random in the range $[-10.5 \text{ mm}, -1 \text{ mm}]$ (i.e., the visible region in the data) and with initial velocities drawn according to the stationary velocity distribution of the OU process. Fig. S8B (Inset) shows a plot of the computed mean displacement $\langle \Delta x(t) \rangle$ and SD in the simulations. Fig. S8B elucidates why no discernible net displacement toward the light source is appreciable in the data, that is, the random motion of *E. gracilis* dominates over the drift toward the source at these spatial and temporal scales. Accordingly, phototactic accumulation of density peaks takes place in a time frame much larger than the typical persistence time $\tau = 1/\gamma = 15 \text{ s}$. Therefore, the model Eq. S5 provides interpretation for the impossibility to observe a net bias toward the source in the experimental trajectories.

The Expansion of the Fokker–Planck Equation. The expansion of the Fokker–Planck equation for the Langevin Eq. S5 in γ^{-1} is acceptable because the typical persistence time $\tau = \gamma^{-1} = 15 \text{ s}$ of the trajectories is much smaller than the typical timescale for the macroscopic dynamics. An intuitive derivation of the expansion can be obtained by neglecting the inertial term \dot{v} in Eq. S5 [a technique known as adiabatic elimination of fast variables (6)], which results in the Langevin equation $\dot{x} = (\sigma/\gamma)\eta(t) + (d\phi/dx)[I(x)]$. The corresponding Fokker–Planck equation describing the time evolution of the probability density function $\rho(x, t)$ is then $(\partial\rho/\partial t)(x, t) = (\sigma^2/2\gamma^2)(\partial^2\rho/\partial x^2)(x, t) - (\partial/\partial x)[(d\phi/dx)[I(x)]\rho(x, t)]$, which is equivalent to Eq. 1 for $D = \sigma^2/(2\gamma^2)$.

Numerical Integration. To compute the time evolution of algal accumulation according to the Keller–Segel model (Fig. 3), we integrated Eq. 1 numerically with the method of lines (7) in the domain $x \in [-6.25, 6.25] \text{ cm}$, whose total length of 12.5 cm corresponds to one period of the periodic light intensity profile established in the experiments. The initial condition was uniform and equal to the mean cell density. Reflecting boundary conditions were set at the border of the domain. Eq. S5 was integrated numerically with the Euler–Maruyama method of order 1/2 to compute the model predicted mean displacement and SD for the experimental settings (Inset in Fig. S8B). The light intensity profile used in the numerical integrations of Eq. 1 and Eq. S5 was the best fit of the equation $I(x) = c_0/(x^2 + c_1^2)^2$, which approximates very well the measured profile (Fig. S1).

SI Discussion

Sensing of Light Directionality Cannot Explain the Data. One might wonder whether a model based on the sensing of the directionality of light propagation, as opposed to its intensity, could explain the experimental results. In our experimental setup, such model would read as follows:

$$\frac{\partial\rho(x, t)}{\partial t} = \frac{\partial}{\partial x} \left[D \frac{\partial\rho(x, t)}{\partial x} - k \text{sign}(x)\rho(x, t) \right], \quad [S6]$$

where the advection velocity is k and the term $\text{sign}(x)$ accounts for the directed movement of cells in the direction of light

propagation (the light source is placed at $x=0$). This model predicts a stationary algal density profile proportional to $\exp(-k/D|x|)$, a cusp centered at the origin, which is in stark contrast with the shape of the experimental algal density distributions and with its dependence on light intensity (Fig. 2 A–G). Fig. 2 A–G shows that, despite the light source being always placed at $x=0$ and the direction of light propagation being thus invariant across the panels, the algal density profiles in the presence of different light intensities are dramatically different, an effect due solely to the variation in light intensity. Thus, at least in our experimental setup, including light intensity in the phototactic potential is necessary to reproduce the observed accumulation patterns and dynamics.

Here, we show that also phototactic models based on the sensing of the directionality of light propagation with an advection velocity dependent on light intensity provide a poor fit to the measured stationary distributions. Specifically, we study the class of models defined by the advection-diffusion equation:

$$\frac{\partial \rho(x,t)}{\partial t} = \frac{\partial}{\partial x} \left[D \frac{\partial \rho(x,t)}{\partial x} - k\eta[I(x)]\text{sign}(x)\rho(x,t) \right], \quad [\text{S7}]$$

which is a generalization of Eq. S6. The phototactic velocity dependence on light intensity is given by $k\eta[I(x)]$. For any $\eta[I(x)]$, the stationary algal density distribution for such model, in the presence of the light intensity profile $I(x)$ (with $x \in [-L, L]$), is equal to the following:

$$\log \frac{\rho(x)}{\rho(-L)} = \frac{k}{D} \int_{-L}^x dy \eta[I(y)]\text{sign}(y). \quad [\text{S8}]$$

Note that Eq. S8 does not predict the data collapse observed in our data (Fig. 4B, *Inset*). The observation of such collapse is already an indication that Eqs. S7 and S8 may not provide a good fit to the experimental data.

To study the performance of Eq. S8 in fitting the data, we fit simultaneously the stationary density distribution data $\log[\rho(x)/\rho(-L)]$ against the function $(k/D) \int_{-L}^x dy \eta[I(y)]\text{sign}(y)$, for all values of I_0 simultaneously. To do so, we minimized the χ^2 :

$$\chi^2 = \sum_{j=1}^7 \int_{-L}^L dx \left[\frac{k}{D} \int_{-L}^x dy \eta[I_{0j}i(y)]\text{sign}(y) - \log \frac{\rho_j(x)}{\rho_j(-L)} \right]^2, \quad [\text{S9}]$$

where I_{0j} identifies the j th value of the experimental peak light intensities and ρ_j is the stationary density distribution measured with peak light intensity I_{0j} . The best fit of Eq. S8 is compared with the best fit of the generalized Keller–Segel model derived in the main text (Eq. 1 of the main text with ϕ as in Eq. 3 of the main text) via the AIC. To perform a fair comparison between models, the best fit of Eq. S8 for various choices of $\eta(I)$ is compared here to the best fit of the generalized Keller–Segel model obtained by minimizing the χ^2 :

$$\chi^2 = \sum_{j=1}^7 \int_{-L}^L dx \left[\frac{1}{D} a I_{0j} i(x) \frac{I_c - I_{0j} i(x)}{I_r + I_{0j} i(x)} - \log \frac{\rho_j(x)}{\rho_j(-L)} \right]^2, \quad [\text{S10}]$$

instead of fitting the phototactic potential $\phi = aI(I_c - I)/(I_r + I)$ from the data collapse of $\log[\rho/\rho(-L)]$ vs. I (Fig. 4B), as was done in the main text.

The functional form for the advection velocity $\eta(I)$ in Eqs. S7 and S8 needs to account for positive phototaxis for I less than a critical value \hat{I} and for negative phototaxis for $I > \hat{I}$. A sketch of such qualitative behavior for the advection velocity is shown in

figure 1 of ref. 8. However, no functional form for the dependence of the advection velocity on I was provided therein. Here, we compare several different choices for $\eta(I)$ chosen to reproduce such behavior. The list of functional forms for $\eta(I)$ investigated here is reported in Table S2. The best-fit parameters of Eq. S8 with $\eta(I)$ as in Table S2 and the corresponding AIC values are reported in Tables S3–S5. Fig. S5 shows the corresponding best fits for the stationary algal distributions at the different experimental peak light intensities I_0 . All of the best fits of Eq. S8 with the different choices of $\eta(I)$ listed in Table S2 have an AIC value much larger than the best fit of the generalized Keller–Segel model with the generalized receptor-law illustrated in the main text. Such result is a strong indication that the generalized Keller–Segel model (Eqs. 1 and 3 of the main text) provides the best description of phototactic behavior in the phytoplankton *E. gracilis*.

Comparison with Previous Models for Phototaxis. Two main phenomenological approaches have been adopted in the literature to model phototaxis of motile algae (8–10), both acknowledging the lack of experimental verification. The first is a photokinetic approach (8, 9, 11), where the average swimming velocity of cells is assumed to be a function of the light intensity I . Vincent and Hill (8) assumed that the average cell velocity in a vertical light gradient is given by $v_p(I) = vT(I)$, where v is the average cell swimming speed and $T(I)$ is a suitable taxis response function (see figure 1 in ref. 8). In the previous section, we showed that this class of models provides an unsatisfactory fit to our data. Analogously, Williams and Bees (9) proposed a photokinetic model in which the average cell velocity is a linear function of I , i.e., $v_p(I) = v/I_c \cdot (I - I_c)$, equal to v in the dark and equal to zero at I_c .

The above model assumptions were taken as working hypotheses due to the lack of direct or indirect empirical validation (8, 9). The need for experimental characterization of the phototactic response to move beyond the linear assumption was clearly stated therein (9). Such models described phototaxis in relatively shallow settings (a few centimeters) where light came uniformly from above and heterogeneity in the light availability would be solely induced by cell shading. In refs. 8 and 9, light was assumed to control the magnitude and the sign of the cell swimming velocity, whereas the directional bias in the vertical direction is provided by gyrotaxis and gravitaxis. Thus, cells were assumed to exhibit no net average displacement in the absence of gravity.

Burkart and Häder (11) performed a light-trap experiment with the alga *Phormidium uncinatum* and used experimental observations to derive an advection model with average cell velocity $v_p[I(x)] = \alpha \log[\beta I(x)]$ (for $I \geq \beta^{-1}$ and with $\alpha > 0$), neglecting cells diffusion. Such a model cannot reproduce the negative phototaxis behavior observed in *E. gracilis*, because v_p is assumed to be a monotonically increasing function of I . Thus, cells would accumulate at the highest available light intensity value, contrary to our experimental results (Figs. 2 E–G and 4D, main text).

A different modeling approach consists of assuming an advection flow proportional to the light intensity gradient, $v_p[dI/dx] = \chi dI(x)/dx$ ($\chi > 0$), such as in Torney and Neufeld (12), where cell aggregation in turbulent flows was investigated theoretically. The proportionality of the advection flow to dI/dx ensures the existence of a net flow toward regions of higher light intensity. However, because v_p is not a function also of the light intensity I , possible saturating effects or photophobic behavior at high light intensities are neglected. The response function chosen by Torney and Neufeld (12) corresponds to the choice $\phi(I) = \phi_1(I) = aI$, which gives a bad fit for the data shown in Fig. 4B, even if only the data points up to $I_m = 5.5 \text{ W}\cdot\text{m}^{-2}$ [maximum of the experimental $\phi(I)$] are used. Specifically, the functional form ϕ_2 performs best compared with ϕ_1 and ϕ_3 ($\Delta\text{AIC}=145$ and 26, respectively), when the data for ϕ (Fig. 4B, main text) are truncated at $I_m = 5.5 \text{ W}\cdot\text{m}^{-2}$.

Other mechanistic approaches have been explored to model phototaxis in combination with gyrotaxis. For example, Williams and Bees (9) considered other two models: one in which cells exhibited a center-of-mass offset dependent on light intensity; and another in which a reactive phototactic torque was introduced. However, because several additional processes are included, comparison of such models with data on photo-bioconvection patterns are difficult and mostly qualitative (10). Williams and Bees (10) provided the first replicated experimental investigation of photo-bioconvection patterns. They found qualitative agreement between the experimental data and the model predictions (9) for the dominant initial wavelength of bioconvective patterns obtained via linear stability analysis (10). Limitations to the quantitative comparison of the models and the experiments are discussed therein (10).

In our experiments, light came from below and cells were observed to distribute mostly on one layer at the top of the channels. Therefore, shading was neglected (unlike in refs. 8 and 9) and light gradients are present by design owing to the experimental setup. The assumption that the phototactic velocity v_p is a function of the light intensity I (and not of I and dI/dx), such as in refs. 8, 9, and 11, is unfeasible here, because it would induce a net phototactic movement in uniform light settings, without the existence of a preferential direction in the horizontal plane. The fact that the advection velocity is a function of both I and dI/dx is a common feature of Keller–Segel models, compare, e.g., equation 1 in ref. 3, and ensures that no net movement is induced in homogeneous distributions of the stimulus (be it a

chemical for chemotaxis or light for phototaxis). Our framework differs from previous attempts to model phototaxis for the fact that the phototactic velocity here is a function of both the light intensity I and its spatial gradient dI/dx , i.e., $v_p = d\phi/dx = d\phi/dI \cdot dI/dx$ (ϕ is a function of I). A model capable of describing both the positive and negative phototaxis regimes (a feature present in refs. 8 and 9 without direct experimental validation, and absent in refs. 11 and 12) is deemed desirable because negative phototaxis has important ecological consequences as it allows cells to avoid harmful radiation. Moreover, mechanisms describing both positive and negative phototaxis contribute to vertical positioning of sensible organisms in the water column (2), a widespread behavior in phytoplankton (13), and were suggested as key components of technological applications, such as harvesting in photobioreactors (www.google.com/patents/US20100237009) and toward the use of microorganisms as micropropellers (14).

Compared with previous research efforts, our investigation allowed a quantitative experimental determination of the phototactic response function (embedded in the potential ϕ and, by derivation, in the advection velocity v_p) directly from cell density patterns in a broad range of light intensities, thus allowing the characterization of both negative and positive phototaxis regimes within a unified mathematical framework. The simple experimental settings devised allowed a direct quantitative comparison of the model with the experiments and invites further experimental investigation in more complex scenarios.

1. Sbalzarini IF, Koumoutsakos P (2005) Feature point tracking and trajectory analysis for video imaging in cell biology. *J Struct Biol* 151(2):182–195.
2. Häder DP, Griebenow K (1988) Orientation of the green flagellate, *Euglena gracilis*, in a vertical column of water. *FEMS Microbiol Ecol* 53(3–4):159–167.
3. Tindall MJ, Maini PK, Porter SL, Armitage JP (2008) Overview of mathematical approaches used to model bacterial chemotaxis II: Bacterial populations. *Bull Math Biol* 70(6):1570–1607.
4. Burnham KP, Anderson DR (2002) *Model Selection and Multimodel Inference: A Practical Information-Theoretic Approach* (Springer, New York), 2nd Ed.
5. Mendez V, Campos D, Bartumeus F (2014) *Stochastic Foundations in Movement Ecology* (Springer, Berlin).
6. Gardiner C (2006) *Stochastic Methods* (Springer, Berlin), 4th Ed.
7. Schiesser W (1991) *The Numerical Method of Lines Integration of Partial Differential Equations* (Academic, San Diego).
8. Vincent RV, Hill NA (1996) Bioconvection in a suspension of phototactic algae. *J Fluid Mech* 327:343–371.
9. Williams CR, Bees MA (2011) Photo-gyrotactic bioconvection. *J Fluid Mech* 678:41–86.
10. Williams CR, Bees MA (2011) A tale of three taxes: Photo-gyro-gravitactic bioconvection. *J Exp Biol* 214(Pt 14):2398–2408.
11. Burkart U, Häder DP (1980) Phototactic attraction in light trap experiments: A mathematical model. *J Math Biol* 10(3):257–269.
12. Torney C, Neufeld Z (2008) Phototactic clustering of swimming microorganisms in a turbulent velocity field. *Phys Rev Lett* 101(7):078105.
13. Jékely G (2009) Evolution of phototaxis. *Philos Trans R Soc Lond B Biol Sci* 364(1531):2795–2808.
14. Itoh A (2004) *Euglena* motion control by local illumination. *Bio-mechanisms of Swimming and Flying*, eds Kato N, Ayers J, Morikawa H (Springer, Tokyo), pp 13–26.

Table S2. Candidate functional forms for $\eta(I)$

$\eta_A(I) = I(1 - \beta I)/(1 + \alpha I)$	$\eta_B(I) = I(1 - \beta I)$
$\eta_C(I) = \log(1 + \gamma I)(1 - \beta I)$	$\eta_D(I) = I[1 - \log(1 + \delta I)]/(1 + \alpha I)$
$\eta_E(I) = I(1 - \log(1 + \delta I))$	$\eta_F(I) = \log[1 + \gamma I]/\log[1 + \delta I]$
$\eta_G(I) = I(1 - \epsilon\sqrt{I})/(1 + \alpha I)$	$\eta_H(I) = I(1 - \epsilon\sqrt{I})$
$\eta_I(I) = \log[1 + \gamma I](1 - \epsilon\sqrt{I})$	

Functional forms for $\eta(I)$ aimed at reproducing the positive phototactic behavior observed at low light intensities and the negative phototactic behavior observed at high light intensities.

Table S3. Best-fit parameters for the simultaneous fit of Eq. S7 to all measured stationary density profiles at different values of I_0 , with different choices for $\eta(I)$: Part 1

Model $\eta_A(I)$		Model $\eta_B(I)$		Model $\eta_C(I)$	
Parameter	Estimate (\pm SE)	Parameter	Estimate (\pm SE)	Parameter	Estimate (\pm SE)
k/D , m/W	-250 ± 7	k/D , m/W	-51 ± 1	k/D , 1/m	-38 ± 1
α , m ² /W	1.63 ± 0.10	β , m ² /W	0.0647 ± 0.0008	β , m ² /W	0.126 ± 0.001
β , m ² /W	0.144 ± 0.002			γ , m ² /W	8.2 ± 0.7
AIC = -683		AIC = 966		AIC = -573	

SEs are computed as the diagonal elements of the inverse Hessian matrix evaluated at the minimum. The AIC values for all choices of $\eta(I)$ are much larger than the AIC value for the best fit of the Keller–Segel model with generalized receptor law (AIC = -1,398.5) performed by minimizing the χ^2 as in Eq. S10, strongly suggesting that Eq. S6 is inadequate to describe the experimental data.

Table S4. Best-fit parameters for the simultaneous fit of Eq. S7 to all measured stationary density profiles at different values of I_0 , with different choices for $\eta(I)$: Part 2

Model $\eta_D(I)$		Model $\eta_E(I)$		Model $\eta_F(I)$	
Parameter	Estimate (\pm SE)	Parameter	Estimate (\pm SE)	Parameter	Estimate (\pm SE)
k , m/W	-218 ± 5	k , m/W	-69 ± 1	k , 1/m	-78 ± 4
α , m ² /W	0.74 ± 0.04	δ , m ² /W	0.131 ± 0.002	γ , m ² /W	3.14 ± 0.22
δ , m ² /W	0.299 ± 0.005			δ , m ² /W	0.269 ± 0.004
AIC = -772		AIC = 698		AIC = -726	

SEs are computed as the diagonal elements of the inverse Hessian matrix evaluated at the minimum. The AIC values for all choices of $\eta(I)$ are much larger than the AIC value for the best fit of the Keller–Segel model with generalized receptor law (AIC = -1,398.5) performed by minimizing the χ^2 as in Eq. S10, strongly suggesting that Eq. S6 is inadequate to describe the experimental data.

Table S5. Best-fit parameters for the simultaneous fit of Eq. S7 to all measured stationary density profiles at different values of I_0 , with different choices for $\eta(I)$: Part 3

Model $\eta_G(I)$		Model $\eta_H(I)$		Model $\eta_I(I)$	
Parameter	Estimate (\pm SE)	Parameter	Estimate (\pm SE)	Parameter	Estimate (\pm SE)
k , m/W	-251 ± 6	k , m/W	-84 ± 2	k , 1/m	-98 ± 5
α , m ² /W	0.71 ± 0.04	ϵ , m/W ^{1/2}	0.273 ± 0.002	γ , m ² /W	2.8 ± 0.2
ϵ , m/W ^{1/2}	0.404 ± 0.003			ϵ , m/W ^{1/2}	0.383 ± 0.002
AIC = -746		AIC = 651		AIC = -687	

SEs are computed as the diagonal elements of the inverse Hessian matrix evaluated at the minimum. The AIC values for all choices of $\eta(I)$ are much larger than the AIC value for the best fit of the Keller–Segel model with generalized receptor law (AIC = -1,398.5) performed by minimizing the χ^2 as in Eq. S10, strongly suggesting that Eq. S6 is inadequate to describe the experimental data.